JOURNAL OF GUIDANCE, CONTROL, AND DYNAMICS
Vol. 23, No. 4, July–August 2000

Drag-Based Predictive Tracking Guidance for Mars Precision Landing

Kuang-Yang Tu,* Mohammad S. Munir,† and Kenneth D. Mease‡
University of California, Irvine, Irvine, California 92697
and
David S. Bayard§
Jet Propulsion Laboratory, California Institute of Technology, Pasadena, California 91109

An atmospheric entry guidance law is developed for a range of low-lift landers consistent with those expected to be flown in NASA's upcoming series of Mars exploration missions. The lander flight path is controlled by bank angle adjustments. The guidance law is a drag-based predictive tracking guidance law similar to that used by NASA's Space Shuttle. Modifications to the Shuttle law are introduced to accommodate the very low-lift capability of the expected landers, as well as additional constraints due to using a fixed trim angle and a low bandwidth attitude control system. Applying the modified guidance law to a representative entry scenario taken from the NASA Mars Surveyor 2001 mission, Monte Carlo simulation results indicate that a lander with a maximum lift-to-drag ratio of only 0.12 can be guided to within 10 km of a specified parachute deployment latitude/longitude point with approximately 99% certainty. Additional dynamic pressure and Mach number constraints required for successful parachute deployment are also shown to be satisfied with approximately 99% certainty. Results for landers with maximum lift-to-drag ratios of 0.18 and 0.06 are included for comparison.

Introduction

AMONG the many complex and challenging future Mars missions such as sample return, in situ science, telerobotic exploration, human exploration, robotic colonization, etc., many are likely to require an advanced guidance, navigation, and control capability for precision landing. In emerging missions, landing sites are typically selected based on their importance to geological and exobiological exploration. The need for precision landing is driven by science objectives to study focused sites of limited radius, where science specimens must either be in immediate proximity of the lander or must be reachable by robotic rovers deployed from the lander base. More complex mission scenarios may require landing close to equipment or cached samples from a previous mission or near a previously established Mars base. Aside from helping to satisfy these basic mission objectives, precision landing also helps to avoid hazardous terrain and reduce landing risks.

As a useful point of departure, one can consider the recent Mars Pathfinder mission, which successfully landed on the surface of Mars on 4 July 1997. The Mars Pathfinder entry was ballistic, meaning that the vehicle generated no lift nominally and that there was no closed-loop entry guidance. Although a specific landing site was targeted, the achieved landing site could only be guaranteed (i.e., to 99.7% confidence) to be inside a 299 × 45 km ellipse, when all potential dispersions were considered.[1,2] Note that rather than using worst-case numbers, targeting decisions for Pathfinder were based on a 95% dispersion ellipse of ±100 km downrange and ±30 km crossrange and that the actual landing error realized for Pathfinder was 27 km.

Figure 1 (photograph obtained from Jet Propulsion Laboratory, California Institute of Technology/NASA web site at http://RMET.jpl.nasa.gov/RMET/exptech/98met/98preciseland.html) shows a potential landing site located in what is believed to be an ancient Martian lake bed. Martian lake beds are of scientific interest due to liquid surface water they might have once held and potential indications of early life forms. The target landing site is shown in the center of a 1-km-radius circle. For comparison purposes, the landing dispersion ellipse associated with the Mars Pathfinder lander is superimposed on Fig 1. It is seen that the level of precision associated with the Pathfinder landing would be inadequate to deliver even the most capable of rovers (of the 10-km class) to the desired science target.

It is true that future Mars missions will benefit from improved approach navigation prior to atmospheric entry. However, even with the best achievable approach navigation available in the near future, the expected dispersions associated with unguided flight in the atmosphere can still be expected to be on the order of 50-km radius (cf., Fig. 1). This motivates moving away from simple ballistic entries and toward more sophisticated entries using closed-loop entry guidance.

Using a combination of closed-loop entry guidance and a low-lift lander [having lift-to-drag ratio (L/D) between 0.6 and 0.18], a desired NASA goal is to be able to land within a 10-km radius of the desired target site.[3] With greater lift capability and better navigation, landing within a 1-km circle may be achievable.

The guidance law documented in this paper is developed for a range of low-lift landers consistent with those expected to be flown in NASA's upcoming sequence of Mars exploration missions. The Mars Surveyor Program 2001 (MSP'01) mission is the first Mars mission expected to attempt precision landing under closed-loop entry guidance. The details of the vehicle definition and problem statement for MSP'01, given by Striepe et al.,[4] are used for the numerical results presented in this paper. The lander is defined to be similar to the 1997 Mars Pathfinder lander, except that the internal mass of the vehicle is distributed such that the vehicle trims at a nonzero angle of attack and generates some lift. (Aside from the geometric layout, the flight control system shares more in common with the MS 1998 lander). The attitude control system is capable of banking the vehicle about its velocity vector and, thus, directing the lift for flight-path control. In Fig. 2 two configurations are considered that differ only by their L/D: one has an L/D of about 0.12 and the other has an L/D of about 0.06. For comparison, another lander configuration with an L/D of about 0.18 is also considered.

We address the guidance problem of commanding the bank angle during the atmospheric entry so that the vehicle reaches a specified

Received 12 February 1999; revision received 19 January 2000; accepted for publication 21 January 2000.

*Postdoctoral Researcher, Department of Mechanical and Aerospace Engineering. Member AIAA.
†Graduate Student, Department of Mechanical and Aerospace Engineering. Student Member AIAA.
‡Associate Professor, Department of Mechanical and Aerospace Engineering. Associate Fellow AIAA.
§Senior Research Scientist, Autonomy and Control Section. Senior Member AIAA.

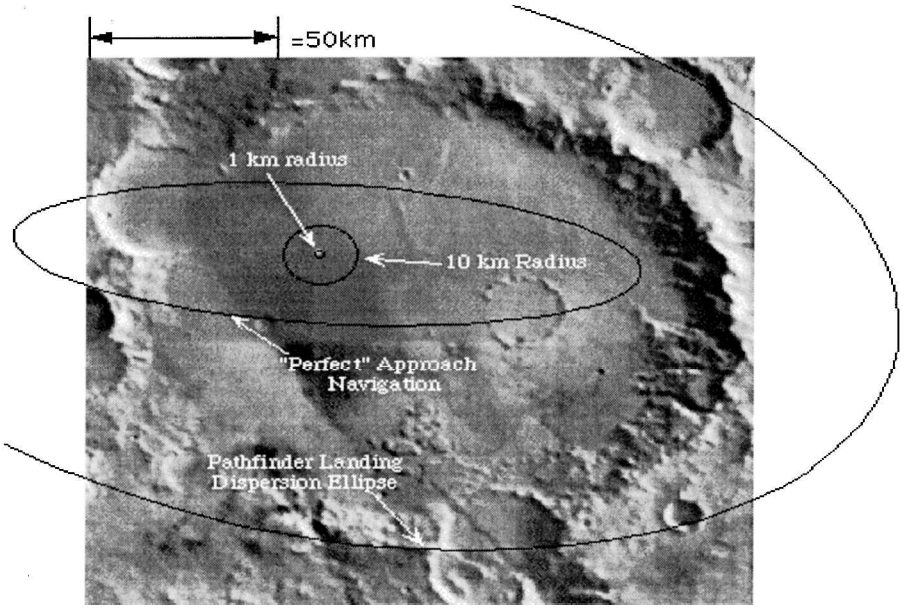

Fig. 1 Gusev crater: a possible landing site.

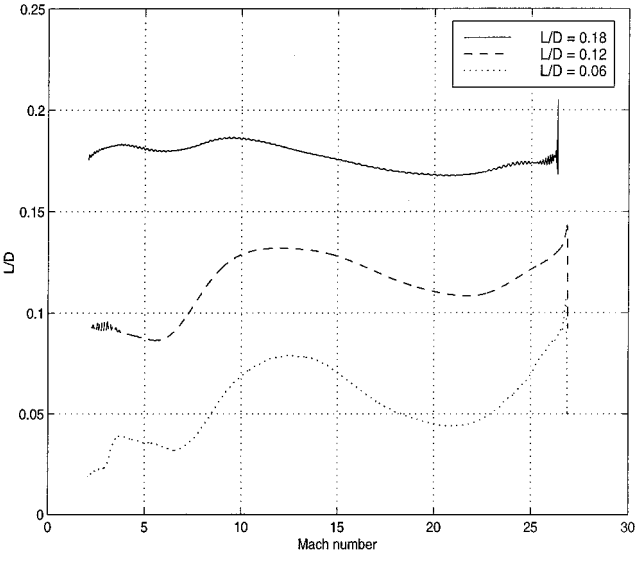

Fig. 2 Lander *L/D* vs Mach number.

parachute deployment condition that includes specifications on latitude and longitude as well as acceptable ranges of dynamic pressure and Mach number. A guidance law is developed that belongs to the class of drag-based predictive tracking guidance that has evolved through the NASA Apollo and Space Shuttle programs[5,6] and other developments.[7–10] The advantages of this class of guidance laws over purely predictive and purely tracking guidance laws are described. Modifications to the Space Shuttle Orbiter entry guidance law[6] are introduced to accommodate the low-lift capability and the combination of a low bandwidth bank angle control system and a fixed trim angle of attack that characterize the Mars landers under consideration.

Guidance Problem Formulation

Equations of Motion

The lander is modeled as an unpowered point mass flying in a stationary atmosphere of a nonrotating planet. The three kinematic and three force equations for the translational motion are[11]

$$\dot{\theta} = \frac{V \cos\gamma \sin\chi}{r \cos\phi} \tag{1}$$

$$\dot{\phi} = (V \cos\gamma \cos\chi / r) \tag{2}$$

$$\dot{r} = V \sin\gamma \tag{3}$$

$$\dot{V} = -D - g \sin\gamma \tag{4}$$

$$\dot{\gamma} = (1/V)\{L \cos\sigma - [g - (V^2/r)]\cos\gamma\} \tag{5}$$

$$\dot{\chi} = (1/V)[(L \sin\sigma/\cos\gamma) + (V^2/r)\cos\gamma \sin\chi \tan\phi] \tag{6}$$

where θ is the longitude, ϕ is the latitude, r is the radial distance from the center of the Mars, V is the velocity, and γ is the flight-path angle. The heading angle is χ, defined as a clockwise rotation angle starting at due north, and σ is the bank angle defined as the angle about the velocity vector from the local vertical plane to the lift vector. An inverse square gravitational acceleration $g = \mu/r^2$, where $\mu = GM_{\text{mars}}$ is assumed. The aerodynamic drag D and lift L accelerations are given by

$$D = \tfrac{1}{2}\rho V^2 (S/m) C_D, \qquad L = \tfrac{1}{2}\rho V^2 (S/m) C_L \tag{7}$$

where ρ is the atmospheric density, S represents the vehicle reference surface area, and m is the mass of the spacecraft. An exponential atmospheric density model,

$$\rho = \rho_r \exp[-(r - r_0)/h_s] \tag{8}$$

is assumed, where ρ_r is the density at the reference radius r_0 and h_s is the constant scale height.

Guidance Objective

The guidance objective during the hypersonic and supersonic phases of entry is to reach a specified latitude and longitude, with an altitude and velocity (actually dynamic pressure) compatible with parachute deployment, at the time when the vehicle energy has decreased to a specified level. The parachute requirements dedicate a feasible region in the altitude–velocity plane.

Guidance Law Design

Drag-Based Predictive Tracking Concept

We employ a drag-based predictive tracking guidance approach.[5–10] It is appropriate to consider energy as the independent variable. We define the specific energy by

$$E = \tfrac{1}{2}V^2 + [(\mu/r_0) - (\mu/r)] \tag{9}$$

where r_0 is a reference surface radius for Mars. Using Eqs. (4) and (9), it can be shown that

$$\dot{E} = -VD \tag{10}$$

Defining range as the distance along the flight path, the predicted range to go is

$$R_p = \int_{t_c}^{t_f} V\,\mathrm{d}t = \int_{E_f}^{E_c} \frac{\mathrm{d}E}{D} \tag{11}$$

where t_c is the current time, t_f is the terminal time, E_c is the current energy, and E_f is the final energy.

Observe that the range, as a function of energy, depends only on the drag profile D. The drag, in turn, can be controlled through the use of the bank angle σ according to the second-order dynamics,

$$D'' = a + bu \tag{12}$$

where D'' denotes the second derivative of D with respect to energy, the term $u = (L/D)\cos\sigma$ acts as a control input, and a and b are functions of the state variables that will be specified later.

The role of the longitudinal guidance law is to command the control input $u = (L/D)\cos\sigma$ such that the vehicle achieves the desired range to target R_t. In this context, a fully predictive guidance approach is one that uses the combined range and drag dynamics to determine the required value of the control at each guidance update. There are several potential problems with this approach:

1) At each time instant the control must be determined not only at the current time, but also over the entire future flight path. This typically causes computational bottlenecks when using general formulations such as those based on optimal control theory. On the other hand, simple formulations (e.g., taking future controls to be constant), reduce computation but may run into state constraints (cf., problem 2, following), or may not be of a rich enough class to generate feasible or desirable entry trajectories.

2) State constraints on dynamic pressure, accelerations, and heating generally make choices of feasible future paths particularly problematic. Although state constraints are not a significant issue for the MSP'01 Lander, they are important for the Space Shuttle[6] and are likely to be necessary for future Mars landers.

3) Calculating the effect of the control inputs on the predicted future flight path requires an accurate aerodynamic force model that is generally not available in practice.

The drag tracking guidance approach is less prone to these problems. A detailed discussion can be found in Ref. 6 (see also more recent generalizations in Refs. 7 and 12). For completeness, a brief overview is included here.

In drag tracking guidance, a drag reference trajectory $D_r(E)$ is planned a priori as a function of energy, and a feedback controller is used to command the bank angle so that the actual drag $D(E)$ tracks $D_r(E)$ during flight. Because the controller is acting simply to null the error between $D(E)$ and $D_r(E)$ in real time, the computation of future controls is avoided completely, that is, overcoming problem 1. If the drag tracking is perfect, it follows from Eq. (11) that the desired range will be achieved.

It has been shown in Ref. 6 that all relevant state constraints for entry can be represented as drag constraints and systematically incorporated into the choice of reference trajectory $D_r(E)$. This overcomes problem 2. Terminal conditions on altitude and dynamic pressure required for successful parachute deployment can be handled by constraining the final value of the drag. In particular, given a nominal trim angle α and fixed aerodynamic and atmospheric density models, the specification of final altitude and dynamic pressure is equivalent to the specification of drag at a final value of energy.

Note that drag causes deceleration, which is measured directly by the accelerometers. In nulling a directly measured error, the drag tracking approach is robust to aerodynamic modeling errors. This overcomes problem 3.

Accordingly, drag tracking largely avoids the aforementioned problems 1–3 and has been the preferred approach in developing NASA's Space Shuttle entry guidance law.

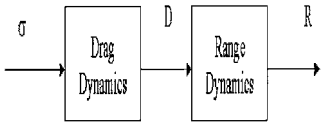

Fig. 3 Cascade structure of longitudinal dynamics.

Issues 1–3 address problems predominatly related to guidance law development. However, other important issues still remain, arising from limited vehicle control authority and actuator constraints. A difficulty that arises in drag tracking is that it places too much faith in the accuracy of drag reference $D_r(E)$ and the controller's ability to track it. For example, errors in physical models and/or entry conditions may render a precomputed $D_r(E)$ difficult to fly. In addition, control errors incurred in tracking the desired drag profile (due to actuator constraints, constraints on vehicle body rates, vehicle lift capability, finite control bandwidth, sensor noise, environmental disturbances, etc.) can induce unacceptably large ranging errors when integrated over time. This motivates the next scheme, which replans $D_r(E)$ at regular intervals during the flight.

In predictive tracking guidance, the reference drag profile is adjusted at regular intervals using Eq. (11) so that the predicted range equals the desired range. As indicated by the cascade structure shown in Fig. 3, the prediction is accurate because the ranging equation Eq. (11) is purely kinematic and does not require force modeling. In the predictive tracking approach, the longitudinal tracking guidance law commands $u = (L/D)\cos\sigma$ (i.e., essentially the vertical component of lift, scaled by the drag) to track the current drag reference D_r. Because $\cos(\sigma) = \cos(-\sigma)$, the sign of the bank angle can be chosen arbitrarily without impacting the longitudinal guidance.

The role of the lateral guidance law is to command the sign of the bank angle σ, which, through Eq. (6), couples into the dynamics and allows one to control heading to meet the desired crossrange requirement. The logic for commanding the sign of the bank angle is based on a heading error corridor. When the lift vector is not in the vertical plane, the heading angle changes. When the vertical plane of motion becomes too different from the vertical plane containing the vehicle and the target, a sign change is commanded. The attitude control system must then rotate the vehicle about the velocity vector for what is termed a bank reversal.

The lateral guidance concept just described has a potential weakness in that the logic is independent of the longitudinal guidance and has second priority. For example, if the longitudinal guidance commands a 0- or 180-deg bank angle, the lateral guidance is left with no control authority. Sufficient lateral control authority can be ensured by constraining the bank angle so that it is bounded away from 0 and 180 deg by some sufficient margin. This is a means of budgeting control authority between the longitudinal and lateral guidance, which has been successfully used in the Space Shuttle program. Note that a combined longitudinal/lateral tracking guidance approach has also been developed for applications where both α and σ can be controlled.[10,12] In the remainder of this section, we describe a particular implementation of the drag-based predictive tracking guidance concept for Mars precision landing. An earlier version of this implementation was documented in a thesis.[13]

For the Space Shuttle Orbiter, the hypersonic L/D is 1.50 and the angle of attack can be adjusted within limits. Although bank angle changes are the primary means of flight-path control, the Shuttle guidance commands angle of attack changes during bank reversals to maintain the desired vertical lift. The features of Mars precision landing that drive our implementation and require some modifications relative to the Shuttle guidance are 1) the lander has a very low L/D ratio, in the range 0.06–0.18; 2) the angle of attack cannot be adjusted to control the flight path; 3) the attitude control system uses 1-lb thrusters, which significantly limits the maximum bank angle rate and acceleration; and 4) the atmospheric density uncertainty along an entry trajectory can be as large as 40%.

Longitudinal Predictive Guidance Design

The longitudinal predictive guidance determines a flyable drag reference that, based on Eq. (11), produces the desired range at a specific terminal energy. The range to the target R_t is taken to be the

straight-line distance from the current position to the target. This straight-line definition of R_t is consistent with that for the predicted range R_p, if the vehicle indeed flies a straight-line path.

In general, the need to plan a reference flight-path angle γ as a function of time can be avoided, if one is flying either near-level flight (i.e., $\gamma = 0$) or a straight-line path to the target. The latter assumption is the appropriate one for the low-lift vehicle under consideration because γ is nominally in the range from -12 to -26 deg.

Drag Reference Initialization

With a sufficiently high L/D, the reference drag profile is limited by vehicle constraints on dynamic pressure, accelerations, and heating.[6,8,9] With a very low L/D, the reference drag profile is limited by the control authority. For the latter case, we choose a constant bank angle near 90 deg in magnitude and determine a trajectory via open-loop simulation using nominal models that achieves the desired range. With a fixed entry position, speed, and heading, the entry flight-path angle can be adjusted to achieve the desired range. The drag profile for this trajectory is taken as the reference drag profile. If the nominal model is without error, then flying the reference requires a 90-deg bank angle, and all of the lifting capability can be used to handle dispersions, that is, off-nominal conditions. Ideally the reference trajectory should also lead to the center of the allowable range of parachute deployment conditions. If the ballistic 90-deg trajectory does not achieve this, then some lift must be used to shape the nominal trajectory. Figure 4 shows an approximation of the boundary of the landing footprint from the nominal entry point to parachute deployment. Conditions for parachute deployment are given later. The boundary is obtained by constant bank angle profiles for the entire range of bank angles. Two particular trajectories are shown: the solid trajectory was generated with $\sigma = 90$ deg and the dotted trajectory was generated with $\sigma = -90$ deg. Because the magnitude of the bank angle is the same for both trajectories, the drag profiles are roughly the same. By executing a bank reversal to change the sign of σ at an appropriate point along either trajectory, final points roughly in between the endpoints of the two trajectories can be reached. To satisfy the parachute deployment criteria, it was determined that the best place to pick a target is in the center of the two terminal points of ± 90 deg as shown in Fig. 4. Either of the drag profiles for the two trajectories can be used as the reference. Note that these reference drag profiles do not include bank reversal effects. We have found that it is best not to include these because of the large variability in where bank reversals actually occur under off-nominal conditions. An Nth-order polynomial representation of the reference drag profile D_r

$$D_r(E) = \sum_{i=0}^{N} C_i E^i \tag{13}$$

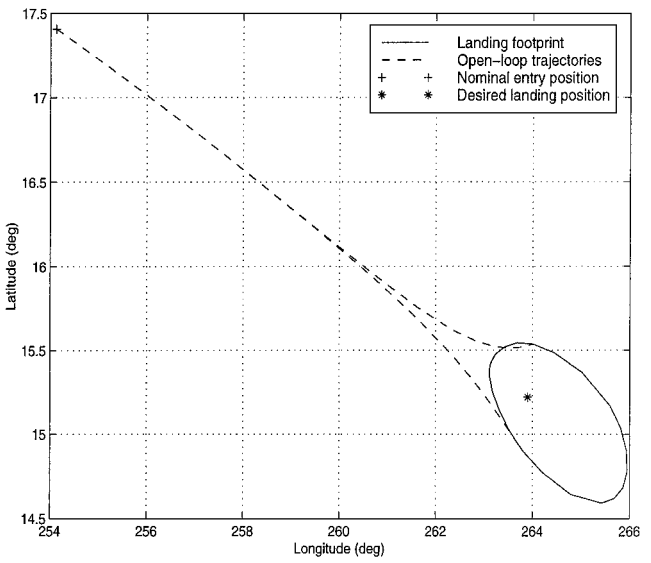

Fig. 4 Landing footprint.

is used to reduce the storage requirements and enable analytic differentiation. A least-squares approximation is used to fit the coefficients C_i to the reference drag profile.

Drag Reference Update

The reference drag profile is updated periodically using a shaping function to null the range error. We use the shaping function,

$$f[x(E)] = 2 - a[x(E) - 0.5]^2 \tag{14}$$

where a is a positive constant and x is a linear function of E given by

$$x(E) = (E - E_c)/(E_f - E_c) \tag{15}$$

Thus, x is equal to 0 at the current energy E_c and is equal to 1 at the terminal energy E_f. Note that the maximum value of the shaping function is 2. The updated reference drag profile is parameterized by the single parameter β as

$$D_r^{\text{ud}}(E) = [1 + \beta f(E)]D_r(E) \tag{16}$$

where D_r^{ud} is the updated reference drag profile. The predicted range to go is calculated by substituting Eq. (16) into Eq. (11) and integrating. The difference between the predicted range to go and the desired range to go is nulled by adjusting β. D_r^{ud} is then fit using the representation in Eq. (13) and becomes the current reference drag profile. This process is repeated at the guidance update interval.

Presently, the time interval between guidance updates is chosen by simulation using trial and error. Empirical evidence suggests that a simple fixed interval is adequate, and performance does not significantly improve when updating more often than some critical period, for example, 20 s in the case study presented later. Nonetheless, more systematic methods (possibly including state-dependent logic) for triggering guidance updates remains as a topic for future research.

The update method just described, based on using shaping functions, has the following attributes. First, it is simple because only a single parameter β is adjusted. Second, the shaping function $f(E)$ can be carefully chosen so that modifications of D_r allow the guidance law to react quickly to needed changes, yet are trackable in the sense that they are consistent with vehicle capability and lie within the limits of available control authority. Further improvement in the update method may be possible, and this is an area for future investigation.

Longitudinal Tracking Guidance Design

The longitudinal tracking guidance law commands the bank angle magnitude $|\sigma|$ as required to track the reference drag profile. It has been shown[7] that nominal exponential tracking, in the absence of control saturation, can be achieved globally by feedback linearization of the drag dynamics, whereas exponential tracking can only be achieved locally using Taylor linearization. Accordingly, the feedback linearization approach is used in the present paper. Aside from potential performance benefits, it is also easier to implement. For example, one does not need to determine a reference γ profile or assume it is zero. A proportional–integral–derivative (PID) law is used to control the nominally linearized drag dynamics. A guidance initiation trigger and a one-sided gain scheduling factor can be added to improve performance, as will be discussed.

PID with Feedback Linearization

The drag dynamics, with E as the independent variable, can be written in the form,

$$D'' = a + bu \tag{17}$$

where

$$u = L\cos\sigma/D \tag{18}$$

$$a = \frac{1}{V^2 D}\left(\frac{[D + g\sin\gamma]\sin\gamma}{h_S} - \left(\frac{1}{h_S} + \frac{2g}{V^2}\right)\right.$$
$$\times\left(-g\cos\gamma + \frac{V^2}{r}\cos\gamma\right)\cos\gamma + D' V^2\left(\frac{\sin\gamma}{h_S} - D'\right)$$
$$\left. + D'[3D + g\sin\gamma] - \frac{2}{V^2}[D + g\sin\gamma]^2\right) \tag{19}$$

$$b = \left(-\frac{1}{h_S} - \frac{2g}{V^2}\right)\frac{\cos\gamma}{V^2} \tag{20}$$

and the first derivative of drag with respect to energy is

$$D' = (\sin\gamma/h_S) + (2/V^2)[D + g\sin\gamma] \tag{21}$$

assuming that terms involving with derivatives of C_D are negligible. Let the drag tracking error be denoted by

$$\Delta D = D - D_r \tag{22}$$

and the first and second derivatives with respect to energy by

$$\Delta D' = D' - D_r' \tag{23}$$

$$\Delta D'' = D'' - D_r'' \tag{24}$$

To achieve closed-loop error dynamics of the linear time-invariant form

$$\Delta D'' + k_1\Delta D' + k_2\Delta D + k_3\int \Delta D\,\mathrm{d}E = 0 \tag{25}$$

where k_1, k_2, and k_3 are constant gains, D'' must satisfy

$$D'' = D_r'' - k_1\Delta D' - k_2\Delta D - k_3\int \Delta D\,\mathrm{d}E \tag{26}$$

Using Eqs. (17) and (26), we obtain the tracking law

$$u_{\mathrm{FL}} = (1/b)(-a + D_r'' - k_1\Delta D' - k_2\Delta D - k_3 z) \tag{27}$$

The integrator state

$$z = \int \Delta D\,\mathrm{d}E$$

is initialized at zero and is rezeroed at each drag update. The first and second derivatives of D_r with respect to E are given by

$$D_r' = \sum_{i=1}^{N} i C_i E^{i-1} \tag{28}$$

$$D_r'' = \sum_{i=2}^{N} i(i-1) C_i E^{i-2} \tag{29}$$

To compute u_{FL} via Eq. (27) and then the σ command via Eq. (18), h_s and μ are obtained from the nominal atmospheric and gravitational models, respectively, and r, V, γ, and L/D are obtained each guidance cycle from the onboard inertial navigation system. D and L/D are estimated directly from inertial measurements, rather than from Eq. (7), to avoid introducing errors from the density and aerodynamic models.

It is emphasized that the closed-loop dynamics Eq. (25) are only achieved under ideal conditions of no mismodeling errors or navigation errors. Some nonidealities (such as drag modeling errors) show up as additional forcing terms on the right-hand side of Eq. (25) that act as disturbances that would bias the tracking error. The integral term in the controller is present to help mitigate such nonideal factors. Other nonidealities such as actuator saturation are more complicated. The reader is referred to Mease and Kremer,[7] where the issue is treated in more detail. Realistic levels of such errors have been injected into all simulations and will be used to evaluate performance in this paper.

One-Sided Gain Scheduling

To accommodate the bank angle rate and acceleration limits and the low L/D, a provision is made to include a one-sided gain scheduling factor in the feedback control law. The gain scheduled version of the control law u_{GS} is

$$u_{\mathrm{GS}} = u_{\mathrm{OP}} + \xi(D)(u_{\mathrm{FL}} - u_{\mathrm{OP}}) \tag{30}$$

where u_{OP} is the open-loop control, $\xi(D)$ is the gain scheduling factor, and u_{FL} is the feedback linearization control law in Eq. (27). The open-loop control is

$$u_{\mathrm{OP}} = L\cos\sigma_{\mathrm{ref}}/D \tag{31}$$

where σ_{ref} is the constant bank angle for the initial reference drag profile.

The gain schedule is denoted as one-sided because it is used to attenuate the control gain only during the early part of the entry trajectory where the dynamic pressure (and, hence, the control lift) is low. This helps to prevent bank angle saturation early on, which reduces latency (due to bank angle turn rate and acceleration limits) in moving to a new attitude more appropriate for the high dynamic pressure region that follows. With this approach, the vehicle is less likely to get caught at an undesirable bank angle (or in the middle of a large maneuver), when the high dynamic pressure segment becomes active.

The gain scheduling factor has the form

$$\xi(D) = (D/D_{\max})^{\eta} \tag{32}$$

where $D_{\max}$ is the expected upper limit for the drag acceleration and η is a positive constant with magnitude larger than one. The gain scheduling factor $\xi(D)$ is, thus, designed to be less than or equal to one. The gain scheduled controller commands the open-loop control u_{OP} when the control authority as indicated by $D/D_{\max}$ is very small early in the entry. As $D/D_{\max}$ increases, the controller is transferred smoothly to the closed-loop controller u_{FL}. Beyond the peak drag the gain scheduling factor is set to one, that is, $u_{\mathrm{GS}} = u_{\mathrm{FL}}$. As the dynamic pressure drops, bank angle saturation again becomes likely, but this time there is no need to interfere because the high dynamic pressure region has already passed.

Implicit Gain Scheduling via Independent Variable

In this section, we investigate the implicit gain scheduling relationship between the time domain and the energy domain closed-loop error dynamics. The following two equations are obtained by applying the chain rule:

$$\Delta\dot{D} = \Delta D'\dot{E} \tag{33}$$

$$\Delta\ddot{D} = \Delta D''\dot{E}^2 + \Delta D'\ddot{E} \tag{34}$$

where $\Delta\dot{D} = \dot{D} - \dot{D}_r$ and $\Delta\ddot{D} = \ddot{D} - \ddot{D}_r$.

Consider the ideal case of feedback linearization (i.e., no mismodeling or navigation errors) where the integral gain is set to zero, that is, $k_3 = 0$. In this case, the time domain closed-loop error dynamics are given by

$$\Delta\ddot{D} + 2\zeta w_n\Delta\dot{D} + w_n^2\Delta D = 0 \tag{35}$$

Using Eqs. (33–35), we obtain the following energy domain closed-loop error dynamics:

$$\Delta D'' + 2\bar{\zeta}\bar{w}_n\Delta D' + \bar{w}_n^2\Delta D = 0 \tag{36}$$

where

$$\bar{\zeta} = \zeta + (\ddot{E}/2w_n\dot{E}) \tag{37}$$

$$\bar{w}_n = (w_n/\dot{E}) \tag{38}$$

If the constant gains $\bar{\zeta}$ and $\bar{w}_n$ are tuned according to the energy domain closed-loop error dynamics, then the following implicit gain

scheduling effect on time domain closed-loop error dynamics can be derived from Eqs. (37) and (38):

$$\zeta = \bar{\zeta} - \left(\ddot{E}/2\bar{w}_n \dot{E}^2\right) \tag{39}$$

$$w_n = \bar{w}_n \dot{E} \tag{40}$$

From Eq. (39), we can see the gain scheduled time domain damping ratio ζ is almost the same as the energy domain damping ratio $\bar{\zeta}$ because $\dot{E}^2 \gg \ddot{E}$. According to Eq. (40), the time domain natural frequency w_n will increase when the absolute value of energy rate $\dot{E}$ increases, which means the controller will be more aggressive while there is more control authority available and less aggressive while there is less control authority. This implicit gain scheduling effect will reduce the likelihood of control saturation.

Lateral Guidance Design

The crossrange is controlled by the sign of the bank angle. A bank (sign) reversal is commanded whenever a dead band boundary, given in terms of the heading error, is reached. The heading error is defined as the angle between the line connecting the vehicle and the target projected onto the local horizontal plane (i.e., the plane perpendicular to the vehicle position vector) and the velocity vector projected onto the same plane. The projection of the velocity vector onto the local horizontal plane is

$$\boldsymbol{V}_P = V\cos\gamma \begin{bmatrix} -\cos\theta\sin\phi\cos\chi - \sin\theta\sin\chi \\ -\sin\theta\sin\phi\cos\chi + \cos\theta\sin\chi \\ \cos\phi\cos\chi \end{bmatrix} \tag{41}$$

The projection of the vector from the current vehicle position X_c to the target position X_t is given by

$$\Delta = X_t - X_c = X_t - r \begin{bmatrix} \cos\theta\cos\phi \\ \sin\theta\cos\phi \\ \sin\phi \end{bmatrix} \tag{42}$$

Its projection onto the local horizontal plane is given by

$$\Delta_p = \left(\frac{X_c}{\|X_c\|} \times \Delta\right) \times \frac{X_c}{\|X_c\|} \tag{43}$$

and the heading error is given by

$$\Delta\chi = \arccos\left(\frac{V_P}{\|V_P\|} \cdot \frac{\Delta_P}{\|\Delta_P\|}\right) \tag{44}$$

The arccos is specified to return an angle in the first quadrant. Next the product

$$\frac{V_P}{\|V_P\|} \times \frac{\Delta_P}{\|\Delta_P\|} \tag{45}$$

is computed, which is also parallel to X_c. However, if

$$\left(\frac{V_P}{\|V_P\|} \times \frac{\Delta_P}{\|\Delta_P\|}\right) \cdot \frac{X_c}{\|X_c\|} \tag{46}$$

is equal to 1, this implies that the two parallel vectors point in the same direction and $\Delta\chi$ is positive, otherwise it is negative. A symmetric heading error corridor is defined by establishing a maximum $\Delta\chi$ as a function of the range to the target R_t. When $\Delta\chi$ reaches this boundary, a bank reversal is commanded.

Additional Guidance Features

The guidance commands to the attitude control system are started when the drag acceleration reaches 5% of the gravitational acceleration. To reserve some control authority for nulling the crossrange error, the bank angle is limited by $|\sigma| \in [\sigma_{\min}, \sigma_{\max}]$ with $0 \le \sigma_{\min} < \sigma_{\max} \le 180$ deg.

Note two other guidance features tested empirically based on experience with the MSP'01 simulation studies: 1) An attempt was made to low-pass filter the drag estimate to remove sensor noise and high-frequency disturbance content (due to local atmospheric density variations) before computing the bank angle command. However, this did not improve performance. Simulations showed there is enough filtering in the system without this, and the additional filter adds unwanted lag to the feedback loop. 2) Special end game logic was tried, involving commanding $\sigma = 180$ deg after inadvertently flying past the target. Although intuitively reasonable, this did not improve on the basic guidance law.

Simulation Results and Analysis

MSP'01 Entry Simulation Testbed

Guidance law performance is assessed using the six-degree-of-freedom (6DOF) Mars landing simulation testbed, described and developed by Striepe et al.[4] and used in the MSP'01 report by Braun et al.[3] This testbed builds on the Program to Optimize Simulated Trajectories (POST),[14] with necessary modifications made to include realistic and detailed mission-specific models. These detailed models include the gravity, planet, atmosphere, aerodynamic data, control system, inertial measurement unit, and mass properties models. Each of these models was carefully checked and their accuracy validated in a variety of tests and comparisons (cf., Ref. 4). Delivery error and knowledge states were used consistent with a navigation update made 5 h prior to the Mars entry interface.

Vehicle Description

As discussed in Ref. 4, the mass of the assumed Mars lander is taken to be 523 kg, with nominal inertia values of $I_{xx} = 261.00$ kg · m^2, $I_{yy} = 194.40$ kg · m^2, $I_{zz} = 212.30$ kg · m^2, and $I_{xy} = I_{xz} = I_{yz} = 0$. A different lateral c.g. offset is chosen for each vehicle studied, consistent with achieving their desired L/D values of 0.18, 0.12, or 0.06, respectively, during the high-drag segment of the entry. The actual variations of L/D with Mach number are shown in Fig. 2.

The attitude control system uses thrusters to augment the damping in the pitch and yaw axes and to respond to bank angle commands from the guidance system. Only 1-lb attitude control thrusters are expected for the MSP'01 lander; the assumed bank angle acceleration $\ddot{\sigma}$ and rate $\dot{\sigma}$ limits are 1.78 deg/s^2 and 20.00 deg/s.

Guidance Parameters

The nominal entry states, the target states at parachute deployment, and the guidance parameters for different lander configurations are given in Table 1.

Table 1 Simulation conditions

	Lander's L/D		
Parameters	0.18	0.12	0.06
ϕ_e, deg	4.90	18.15	18.15
θ_e, deg	159.97	250.34	250.34
h_e, km	243.27	237.39	237.39
V_e, m/s	6,555.85	6,692.33	6,692.33
γ_e, deg	−19.84	−17.35	−17.35
χ_e, deg	107.85	100.69	100.69
ϕ_t, deg	−0.04	13.76	13.73
θ_t, deg	174.95	269.05	269.16
Mach limits	[1.60, 2.28]	[1.60, 2.28]	[1.60, 2.28]
Qbar limits	[400, 1,175]	[400, 1,175]	[400, 1,175]
k_1	0.42	0.42	0.42
k_2	0.044	0.044	0.044
k_3	0.02	0.00	0.00
$\sigma_{\min}$, deg	17	14	13
$\sigma_{\max}$, deg	160	166	167
$D_{\max}$	170	150	150
σ_{ref}, deg	75	94	90
h_s, m	10,000	10,000	10,000
a	2.83	2.83	2.83
N	6	6	6
η	7.00	0.00	2.80
t_{peak}, s	140	150	150
$\Delta\chi_1$, deg	6.00	1.50	0.50
$\Delta\chi_2$, deg	3.00	0.75	0.25
$\Delta\chi_3$, deg	1.50	0.35	0.13

Each simulated entry is terminated at the point of parachute deployment according to the following logic. The parachute is deployed in the altitude range 6.50–17.00 km. If the descending vehicle reaches the upper altitude bound with $V \leq 503.80$ m/s, the parachute is deployed. Otherwise, the parachute is deployed when $V = 503.80$ m/s or $h = 6.50$ km, whichever occurs first.

The guidance law uses the parameter values shown in Table 1. Guidance updates are made every 20 s. The value of β in the guidance update law Eq. (16) is not allowed to exceed 0.05, and so the change in D_r at each update is limited to 10%.

The initial reference bank σ_{ref} is a constant for each lander. The heading error corridor is specified by a maximum $\Delta\chi$ of $\Delta\chi_1$ deg for $R_t > 200$ km, $\Delta\chi_2$ deg for 100 km $< R_t \leq 200$ km, and $\Delta\chi_3$ deg for $R_t \leq 100$ km. One-sided gain scheduling and integral feedback were found to be beneficial for some simulations studied here.

Theoretical Corridors, Expected Errors, and Achieved Corridors

Robustness will be discussed using the notion of corridors. Sensitivity to two key parameters are considered: the entry flight-path angle γ_e, whose nominal value is -17.35 deg (at an assumed altitude of 237.39 km), and a constant multiplier c_ρ on the atmospheric density, whose nominal value is unity. For all corridor studies considered, the L/D of the vehicle is taken to be 0.12, and simulations are performed on the testbed described in Ref. 4.

The theoretical corridor associated with a given parameter is defined as the maximum interval about its nominal value for which precision landing (defined by the position at parachute deployment) to 10-km accuracy is still achievable given the theoretical limits of the vehicle capability. The theoretical corridor is found by using the full lift in the vertical plane (up or down as appropriate) to offset perturbations. Its main use is to quantify fundamental limits on vehicle performance independently of any choice of guidance law.

The theoretical corridor for γ_e is found to be $[-1.50, 0.80]$ deg about its nominal value of -17.35 deg. The theoretical corridor for c_ρ is found to be [0.30, 5.80] (considered as a multiplicative factor) about its nominal value of unity.

For the landing problem to be feasible (irrespective of guidance law used), it is necessary that the theoretical corridor be larger than the expected errors. The largest expected control error in γ_e is $[-0.23, 0.23]$ deg (Ref. 4). This is well within the theoretical corridor of $[-1.50, 0.80]$ deg. The expected worst-case knowledge error for c_ρ is altitude dependent.[4] In the altitude range where the important guidance actions are executed, a representative worst-case error for c_ρ is [0.60, 1.40], that is, ±40% of nominal. This is also within the theoretical corridor of [0.30, 5.80].

Knowing that the problem is feasible, the next step is to assess guidance performance. For a specified guidance law, an achieved corridor is defined by a series of closed-loop control simulations, where the parameter of interest is varied over a range of values (all other variables being held fixed at their nominal values). The achieved corridor is then defined by the lower and upper boundaries of the parameter beyond which a 10-km accuracy is not achievable. Clearly, a guidance law will be robust to a particular parameter variation if the achieved corridor is larger than that parameter's expected error range.

For γ_e, the achieved corridor (associated with drag-based predictive tracking guidance law) is found to be $[-0.70, 0.40]$ deg, which covers the expected error range of $[-0.23, 0.23]$ deg. For c_ρ, the achieved corridor is [0.30, 2.00], which covers its expected error range of [0.60, 1.40]. With this result, the guidance law is empirically found to be robust to expected variations in both entry flight-path angle and atmospheric density. A more comprehensive robustness evaluation, considering simultaneous errors in flight-path angle, atmospheric density, and many other variables, is accomplished by Monte Carlo simulations as described next.

Monte Carlo Simulations

100-Run Case Study

A 100-run Monte Carlo study using the simulation testbed[4] was first performed for each the three different values of $L/D = 0.18$, 0.12, and 0.06 using the drag-based predictive tracking guidance law. Rigorously speaking, 100 runs is not a large enough sample to be statistically significant to a desired 95% confidence. Nevertheless, this study is included because it provides a rough comparison of guidance performance among all three L/D values.

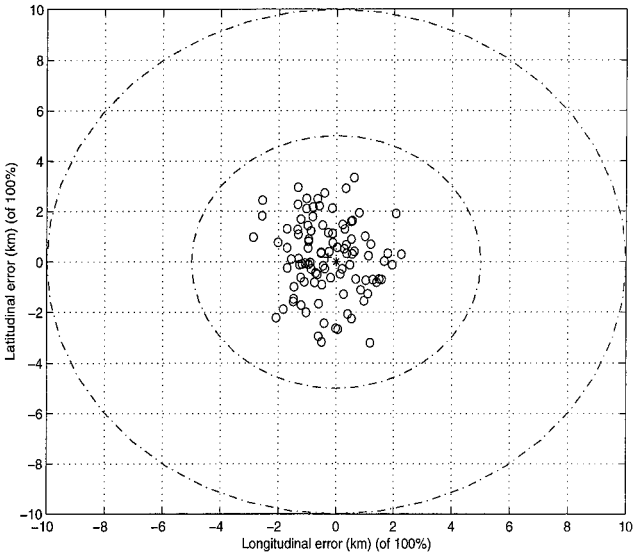

Fig. 5 Total landing errors for six-DOF 100 run (L/D = 0.18).

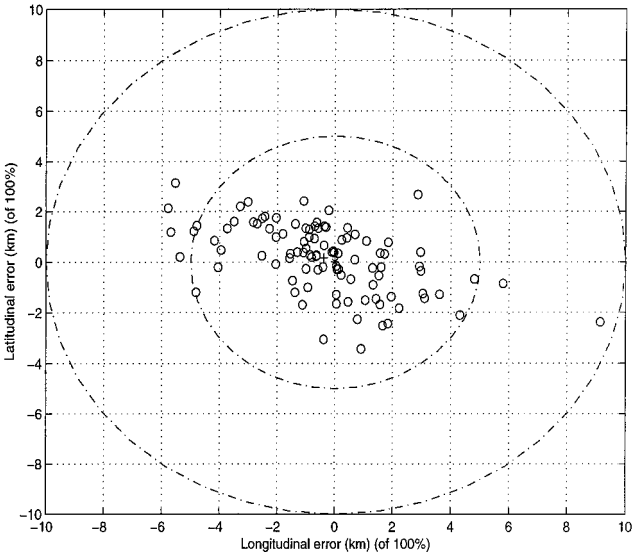

Fig. 6 Total landing errors for six-DOF 100 run (L/D = 0.12).

The total landing errors for each 100-run study are shown in Figs. 5–7, for the values of $L/D = 0.18, 0.12$, and 0.06, respectively. The 100% maximum landing dispersions are 3.50, 9.30, and 11.50 km and the rms total landing errors are 1.90, 3.30, and 4.20 km, respectively. As expected, this indicates a degradation in performance as the vehicle maneuvering capability is reduced.

2000-Run Case Study

Next, a 2000-run Monte Carlo study was performed. The 2000-run study is statistically significant to between 95 and 99% confidence. Full details behind these simulations, including robustness studies and comparison statistics with other state-of-the-art guidance laws, can be found in the report by Braun et al.[3] Hence, only a brief summary is included here. In this study, a desired parachute deployment dynamic pressure (Qbar) range (400–1175 N/m^2), Mach number range (1.60–2.28) and a desired maximum deceleration limit (15 Earth g) are considered as part of the performance characterization. In each case following, 1% of the worst runs are discarded for plotting and discussion purposes that is, eliminating 20 of the total 2000 runs.

For the $L/D = 0.12$ lander, the 20 discarded cases comprise 11 cases that violate the Qbar–Mach constraints and 9 cases with the

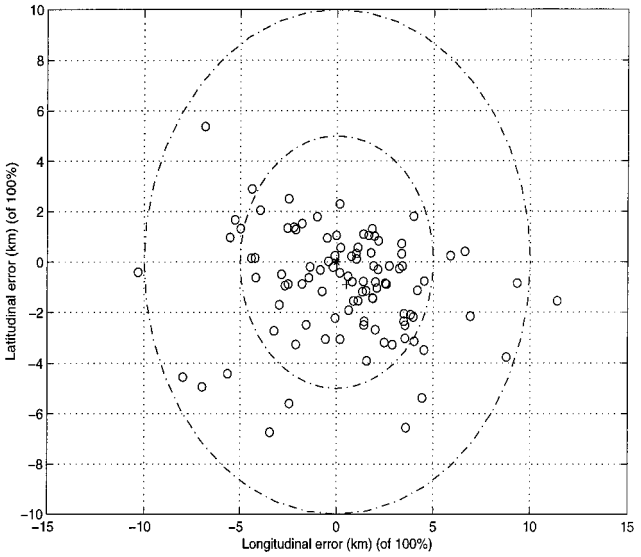

Fig. 7 Total landing errors for six-DOF 100 run (L/D = 0.06).

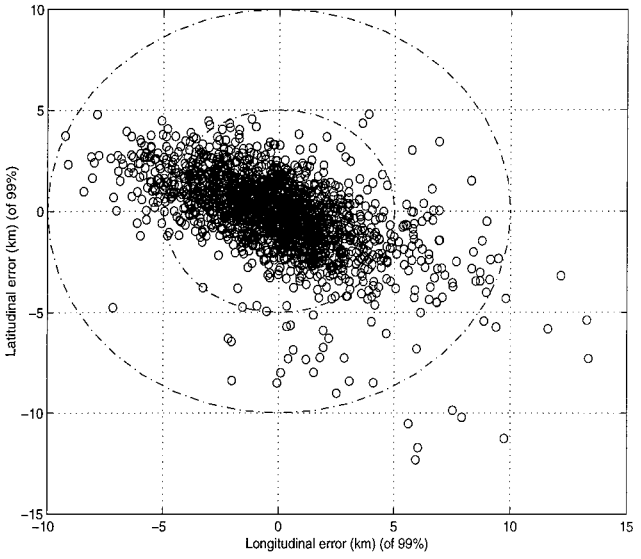

Fig. 8 Total landing errors for six-DOF 2000 run (L/D = 0.12).

worst total landing error. Figure 8 shows the total landing error, where each small circle corresponds to the landing location for one of the simulated entries. The dash–dotted large circle is the 10-km-radius circle. The maximum landing error is 14.80 km. The rms total landing error is 3.30 km.

For the $L/D = 0.06$ lander, the 20 discarded cases comprise 14 cases that violate the Qbar–Mach constraints and the 6 cases with the worst total landing error. Figure 9 shows the total landing error. The maximum landing error is 22.80 km. The rms total landing error is 5.60 km.

If all 2000 Monte Carlo cases are considered (i.e., without discards), the original goal of achieving precision landing to within 10 km of the target (defined by point of parachute deployment) can be achieved with approximately 99 and 94% certainties for $L/D = 0.12$ and 0.06, respectively, while satisfying both the Qbar and Mach number constraints. These percentages drop to 96 and 94%, respectively, when considering trajectories that additionally satisfy the 15-g deceleration limit.

As a useful data point, the percentages are significantly degraded to approximately 25% if no precision guidance is used, that is, if one flies a simple ballistic trajectory. Similarly, whereas the Qbar–Mach number constraints for parachute deployment are satisfied with 99% when using precision guidance, these percentages drop to approximately 76% without precision guidance.

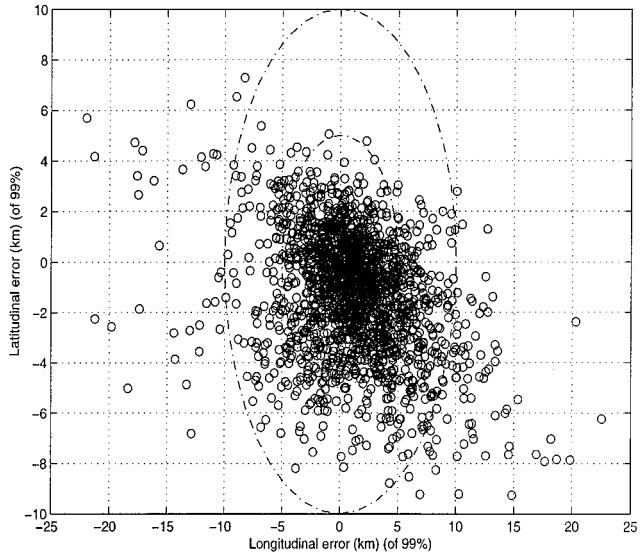

Fig. 9 Total landing errors for six-DOF 2000 run (L/D = 0.06).

Additional simulations studying robustness to anomalies, such as large delivery errors, dust storms, extreme density shears, drops in lift, accelerometer degradation/failure and thruster failure, can be found in Ref. 3.

Conclusions

An overview of and the motivation for drag-based predictive tracking guidance was presented. The guidance concept is applicable to a wide range of low to high L/D vehicles that must land accurately on a planet with an uncertain atmosphere. An implementation for very low L/D vehicles was then developed in detail and analyzed. Monte Carlo results for a Mars landing scenario showed that, for landers with maximum L/D of 0.12 and 0.06, a specified parachute deployment latitude/longitude point can be achieved to within 10-km accuracy with approximately 99 and 94% certainty, respectively, while satisfying dynamic pressure and Mach number constraints needed for successful parachute deployment.

As a separate issue, the guidance law was found to be effective at meeting imposed constraints. Approximately 99% of all trajectories (regardless of L/D) satisfied the desired dynamic pressure and Mach number constraints. A corridor study indicated that the guidance law is robust to expected perturbations in entry flight-path angle and in atmospheric density.

The performance results indicate that the drag-based predictive tracking guidance approach, with the modifications introduced in this paper, provides a viable guidance law for precision landing of entry vehicles with very low-lift capability. The ability of this drag-based guidance approach to accommodate heating, acceleration, and dynamic pressure constraints is an additional attribute expected to be important for future planetary sample return and human missions.

Acknowledgments

This research was supported by NASA. The vehicle and environmental mathematical models and landing simulation used in our research were supplied by the Mars Surveyor Program 2001 Mission Atmospheric Flight Team led by R. Braun, NASA Langley Research Center. The support of this team is gratefully acknowledged. The authors acknowledge the contributions to this work by other members of the Jet Propulsion Laboratory, California Institute of Technology Mars Precision Landing technology development team: D. Farless, A. Ahmed, S. Ploen, and R. Smith (University of California, Santa Barbara). Helpful discussions with C. Graves Jr. and L. Bryant of the NASA Johnson Space Center are also acknowledged.

References

[1] Vaughan, R. M., Kallemeyn, P. H., and Spencer, D. A., "Navigation Flight Operations for Mars Pathfinder," American Astronomical Society, Paper AAS-98-145, Feb. 1998.

[2] Spencer, D. A., and Braun, R. D., "Mars Pathfinder Atmospheric Entry:

Trajectory Design and Dispersion Analysis," *Journal of Spacecraft and Rockets*, Vol. 33, No. 5, 1996, pp. 670–676.

[3]Braun, R. D., Stiepe, S. A., Queen, E. M., Powell, R. W., Cheatwood, F. M., Spencer, D. A., Bayard, D. S., Mase, R., Smith, J., Lyons, D., Farless, D., Carman, G. C., Bryant, L. E., Carpenter, J. R., Graves, C., Ives, D., Ro, T., Willcockson, W. H., Johnson, M. A., Cuseo, J., Kelecy, T., Lander, E., Mease, K. D., Tu, K. Y., Justus, C. G., and Aguirre, J. T., "Mars Surveyor Program 2001 Atmospheric Flight Team Report," NASA TR (to be published).

[4]Striepe, S. A., Queen, E. M., Powell, R. W., Braun, R. D., Cheatwood, F. M., Aguirre, J. T., Sachi, H. A., and Hyons, D. T., "Development of an Atmospheric Guidance Algorithm Testbed for the Mars 2001 Orbiter and Lander," AIAA Paper 98-4570, Aug. 1998.

[5]Bryson, A. E., Jr., "Guidance and Navigation for Entry Vehicles," NASA SP-8015, Nov. 1968.

[6]Harpold, J. C., and Graves, C. A., Jr., "Shuttle Entry Guidance," *Journal of the Astronautical Sciences,* Vol. 27, No. 3, 1979, pp. 239–268.

[7]Mease, K. D., and Kremer, J. P., "Shuttle Entry Guidance Revisited Using Nonlinear Geometric Methods," *Journal of Guidance, Control, and Dynamics,* Vol. 17, No. 6, 1994, pp. 1350–1356.

[8]McEneaney, W. M., and Mease, K. D., "Error Analysis for a Guided Mars Landing," *Journal of the Astronautical Sciences,* Vol. 39, No. 4, 1991, pp. 423–445.

[9]Lu, P., "Entry Guidance and Trajectory Control for Reusable Launch Vehicle," *Journal of Guidance, Control, and Dynamics,* Vol. 20, No. 1, 1997, pp. 143–149.

[10]Bharadwaj, S., Rao, A. V., and Mease, K. D., "Entry Trajectory Tracking Law via Feedback Linearization," *Journal of Guidance, Control, and Dynamics,* Vol. 21, No. 5, 1998, pp. 726–732.

[11]Vinh, N. X., Busemann, A., and Culp, R. D., *Hypersonic and Planetary Entry Flight Mechanics*, Univ. of Michigan Press, Ann Arbor, MI, 1980, pp. 26–28.

[12]Mease, K. D., Teufel, P., Schoenenberger, H., Chen, D. T., and Bharadwaj, S., "Reentry Trajectory Planning for a Reusable Launch Vehicle," AIAA Paper 99-4160, Aug. 1999.

[13]Munir, M. S., "Entry Guidance Law for a Low Lift/Drag Mars Precision Landing," M.S. Thesis, Dept. of Mechanical and Aerospace Engineering, Univ. of California, Irvine, CA, Sept. 1997.

[14]Bauer, G. L., Cornick, D. E., and Stevenson, R., "Capabilities and Applications of the Program to Optimize Simulated Trajectories (POST)," NASA CR-2770, Feb. 1977.